J. Fluid Mech. (2011), *vol.* 670, *pp.* 301–325. © Cambridge University Press 2011
doi:10.1017/S002211201000529X

Vorticity inversion and action-at-a-distance instability in stably stratified shear flow

A. RABINOVICH[1], O. M. UMURHAN[2,3], N. HARNIK[1], F. LOTT[4] AND E. HEIFETZ[1]†

[1]Department of Geophysics and Planetary Sciences, Tel-Aviv University, Tel-Aviv 69978, Israel

[2]School of Mathematical Sciences, Queen Mary, University of London, London E1 4NS, UK

[3]Department of Astronomy, City College of San Francisco, San Francisco, CA 94112, USA

[4]Laboratoire de Météorologie Dynamique, École Normale Supérieure, 24 rue Lhomond, 75231 Paris CEDEX 05, France

(Received 17 February 2010; revised 24 August 2010; accepted 5 October 2010; first published online 14 January 2011)

The somewhat counter-intuitive effect of how stratification destabilizes shear flows and the rationalization of the Miles–Howard stability criterion are re-examined in what we believe to be the simplest example of action-at-a-distance interaction between 'buoyancy–vorticity gravity wave kernels'. The set-up consists of an infinite uniform shear Couette flow in which the Rayleigh–Fjørtoft necessary conditions for shear flow instability are not satisfied. When two stably stratified density jumps are added, the flow may however become unstable. At each density jump the perturbation can be decomposed into two coherent gravity waves propagating horizontally in opposite directions. We show, in detail, how the instability results from a phase-locking action-at-a-distance interaction between the four waves (two at each jump) but can as well be reasonably approximated by the interaction between only the two counter-propagating waves (one at each jump). From this perspective the nature of the instability mechanism is similar to that of the barotropic and baroclinic ones. Next we add a small ambient stratification to examine how the critical-level dynamics alters our conclusions. We find that a strong vorticity anomaly is generated at the critical level because of the persistent vertical velocity induction by the interfacial waves at the jumps. This critical-level anomaly acts in turn at a distance to dampen the interfacial waves. When the ambient stratification is increased so that the Richardson number exceeds the value of a quarter, this destructive interaction overwhelms the constructive interaction between the interfacial waves, and consequently the flow becomes stable. This effect is manifested when considering the different action-at-a-distance contributions to the energy flux divergence at the critical level. The interfacial-wave interaction is found to contribute towards divergence, that is, towards instability, whereas the critical-level–interfacial-wave interaction contributes towards an energy flux convergence, that is, towards stability.

Key words: atmospheric flows, stratified flows

1. Introduction

Recently Harnik *et al.* (2008) developed a 'buoyancy–vorticity wave interaction approach' to describe the linear dynamics of stably stratified shear flows. The essence

† Email address for correspondence: eyalh@post.tau.ac.il

https://doi.org/10.1017/S002211201000529X Published online by Cambridge University Press

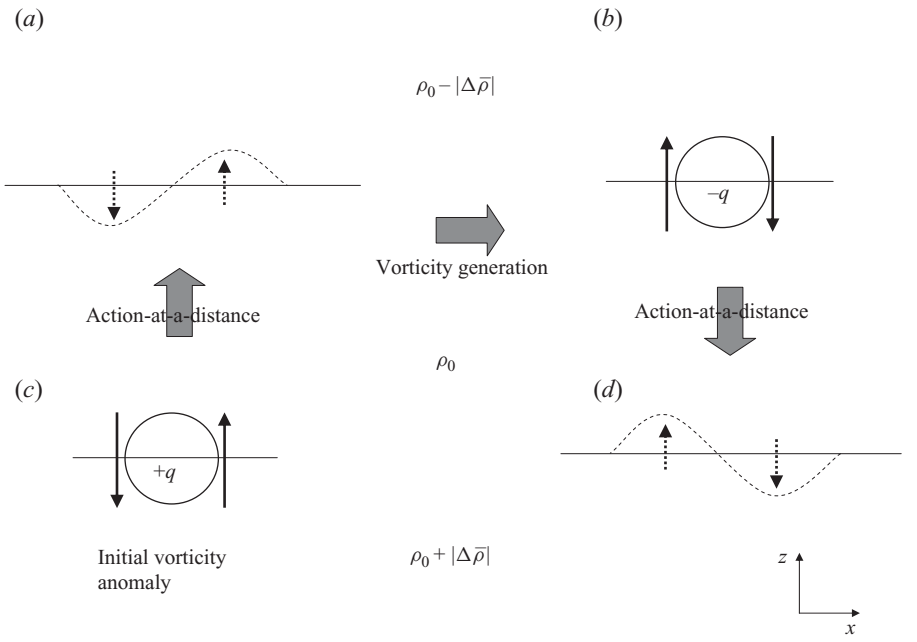


FIGURE 1. The evolution of perturbations on a fluid of three density layers at time (*a*, *c*) t_0 and (*b*, *d*) $t_0 + \Delta t$. An initial vorticity anomaly on an interface between two density layers (*c*) induces a far field velocity which perturbs other interface levels (*a*). These new displacement (buoyancy) anomalies generate vorticity locally (*b*) with an action-at-a-distance effect as well (*d*). As a result, a new material perturbation is formed, altering the initial vorticity anomaly. The large arrows represent the local vertical velocity resulting from the vorticity anomaly, while the small dashed arrows are the vertical velocity induced by a remote layer.

of their view is that in stably stratified flows the buoyancy acts as a restoring force, and therefore a horizontal (say zonal) gradient of material displacement generates vorticity in the meridional direction. By inversion such an initial localized vorticity anomaly at some particular layer induces a non-local vertical velocity field which deforms the flow at remote layers, generating vorticity in the far field. The latter, in turn, induces a far-field velocity which deforms the initially perturbed layer and consequently alters the initial vorticity anomaly (figure 1). Thus, even in the absence of a mean vorticity gradient, vorticity inversion and action-at-a-distance are at the heart of stratified shear flow dynamics.

In barotropic and baroclinic shear flows the basic (potential) vorticity building blocks which interact at a distance are the counter-propagating Rossby waves or CRWs (Bretherton 1966; Hoskins, Mcintyre & Robertson 1985). In stratified shear flows the basic building blocks at each level are mixed gravity–Rossby-wave kernels that, in the absence of shear curvature, are reduced to two oppositely propagating internal gravity wave vortex sheets. The fact that at each given level two building blocks exist (rather than one CRW kernel in the barotropic/baroclinic case) complicates the dynamics; however this is a direct consequence of the interplay between the buoyancy and vorticity fields.

The two necessary conditions for modal instability of barotropic and baroclinic shear flows are straightforwardly rationalized from the CRW perspective. Mutual amplification between two CRWs are possible only if the mean vorticity gradient

https://doi.org/10.1017/S002211201000529X Published online by Cambridge University Press

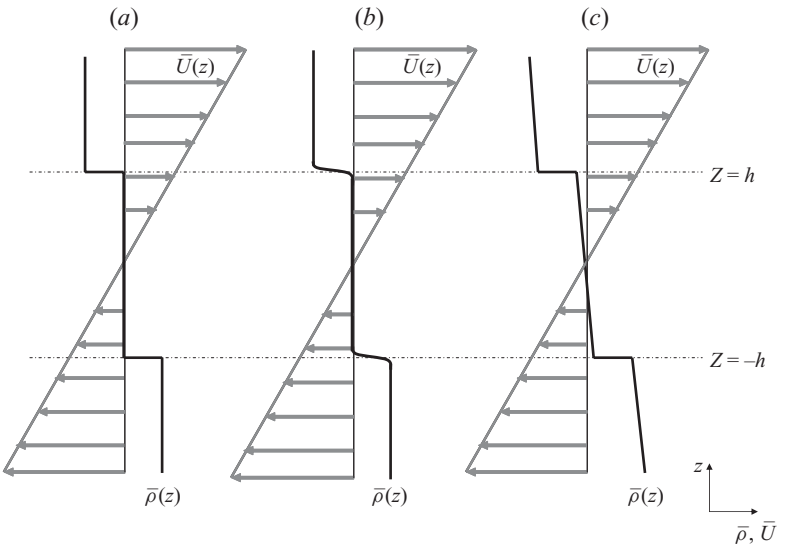


FIGURE 2. The mean density and shear profiles (thick black contours and grey contours with arrows respectively) of the models analysed in this work: (*a*) two density jumps; (*b*) a similar, yet continuous, density profile (see Appendix A); and (*c*) two density jumps with a small ambient density gradient.

at their vicinities changes sign – the barotropic Rayleigh (1880) and the baroclinic Charney & Stern (1962) conditions. The Fjørtoft (1950) condition states that the mean vorticity gradient should be positively correlated with the mean velocity profile, as measured with respect to the point of zero vorticity gradient. When this condition is satisfied the CRWs are able to counter-propagate against the shear, which allows them to phase lock in their constructive interaction configuration. It is thus easy to understand why these conditions may be irrelevant to a stratified shear flow. The mechanism of vorticity anomaly generation by horizontal buoyancy gradients is independent of the presence of mean vorticity gradients. Furthermore, at every layer one of the two gravity wave kernels (propagating in opposite directions in the mean flow frame of reference) is always counter-propagating against the mean flow. Moreover, the Rayleigh and Fjørtoft conditions result, respectively, from the global conservation of pseudo-momentum and pseudo-energy (Shepherd 1990). The equivalent Miles–Howard (M–H; Howard 1961; Miles 1961) necessary condition for stratified shear flow instability (that the Richardson number should be smaller than a quarter somewhere within the domain) does not seem to result from an eddy-associated global conservation law, and therefore it is more challenging to interpret. One of the main aims of this study is to gain a deeper insight on this condition from the kernel gravity wave (KGW) interaction standpoint.

The mechanistic picture of the simple barotropic Rayleigh (1880) and the baroclinic Eady (1949) models, in terms of a two-CRW interaction (Davies & Bishop 1994; Heifetz *et al.* 1999), served as a guiding line in much more complex shear flows (Heifetz *et al.* 2004), including the nonlinear eddy life cycles on realistic jets (Methven *et al.* 2005). Here we follow the same route and examine in detail an equivalent simple model for a stratified shear flow of two density jumps in the presence of constant shear (figure 2*a*). This set-up, examined already by Taylor (1931) and Goldstein (1931), is even simpler than the model of Holmboe (1962), often invoked to address

https://doi.org/10.1017/S002211201000529X Published online by Cambridge University Press

basic questions in stratified shear flows. In some senses, the following analysis is similar to those done in the previous works on shallow water by Hayashi & Young (1986), Sakai (1989) and Knessl & Keller (1992). In their models the instability is also rationalized in terms of action-at-a-distance interaction between localized counter-propagating waves, when the Rayleigh criterion is not satisfied. After formulating the problem and briefly reviewing the buoyancy–vorticity KGW interaction approach (§ 2) we analyse, in detail, the four-KGW interaction of this problem (§ 3). As expected the instability is dominated by the two counter-propagating kernels; however for long wavelengths the other two pro-propagating waves, which must be hindered, contribute as well to the solution.

The common interpretation for the M–H condition stems from the over-reflection perspective, which is based on a cross-shear wave propagation view. When analysing the index of refraction of wave propagation across the shear in the Taylor–Goldstein equation Lindzen & Barker (1985) found that the wave geometry which allows over-reflection, and hence instability, must include a critical level (hereafter CL) which separates between the wave propagation and wave evanescence regions. To obtain an evanescence region at the vicinity of a CL one must have local values of the Richardson number which are smaller than a quarter (Booker & Bretherton 1967). Alternatively, Baines & Mitsudera (1994; see also Baines 1998, chapter 4) used a wave interaction approach, similar to our KGW interaction, but they interpreted the suppression of the instability in terms of absorption of the two waves at the CL between them (a cross-shear wave propagation view). Here we interpret this stabilizing effect of the CL purely in terms of counter-propagating kernel–wave interaction.

The M–H condition is obviously satisfied in the simple set-up of the two density jumps, since the Richardson number is concentrated in two delta functions there (a continuous density profile with two sharp density gradients reveals the same behaviour, as shown in Appendix A). When increasing slightly the stratification elsewhere so that the ambient Richardson number increases from zero to a quarter, the instability is suppressed, in agreement with the M–H condition. Nonetheless, it seems counter-intuitive that such weak ambient stratification (a normalized value of one quarter compared with delta functions) will dominate over the dynamics of the density jumps. In § 4 we analyse the destructive effect of the CL consistently from the buoyancy–vorticity action-at-a-distance approach. It is shown how the KGWs at the density jumps generate vorticity at the CL which acts to mask the constructive interference between the KGWs in the far field. We discuss these results in § 5.

2. KGW formulation for stratified shear flow

We consider an inviscid incompressible Boussinesq two-dimensional flow in the zonal–vertical (x–z) plane, with a zonally uniform basic state that varies only with height and is in hydrostatic balance. For this set-up the linearized momentum and continuity equations become

$$\frac{\mathrm{D}u}{\mathrm{D}t} = -\overline{U}_z w - \frac{1}{\rho_0}\frac{\partial p}{\partial x}, \tag{2.1a}$$

$$\frac{\mathrm{D}w}{\mathrm{D}t} = b - \frac{1}{\rho_0}\frac{\partial p}{\partial z}, \tag{2.1b}$$

https://doi.org/10.1017/S002211201000529X Published online by Cambridge University Press

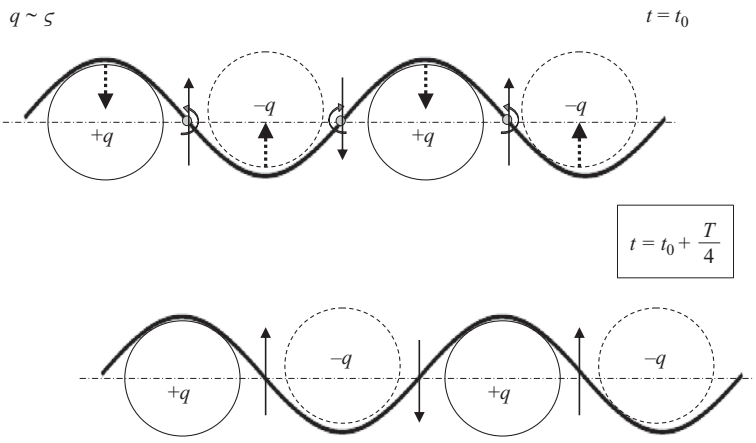


FIGURE 3. The gravity wave mechanism for a ζ^+ wave in a single-jump configuration. The wavy contour represents the displacement, while the positive and negative vorticities are shown with the regular and dashed circles respectively. Notice that the vorticity and the displacement are in phase as the KGW formulation prescribes for the 'plus' kernel. The top wave is for a random time, $t=t_0$, and the bottom wave is the same wave after a fourth of its period, $t=t_0+T/4$. The dashed thick arrows show the buoyancy force on the wave, which is simply the tendency of the disturbances to level out to equilibrium. The solid filled circles mark the axis points which rotate in the direction of the circular arrows as a result of the levelling motion. These points have zero vorticity at $t=t_0$ but generate the most vorticity with time and are also the points of maximum vertical velocity marked with the thin long arrows. Taking into consideration all of the processes in the scheme – interface displacement due to the vertical velocity and the flattening accompanied by generation of new vorticity – accounts for the rightward phase propagation depicted.

$$\frac{\mathrm{D}b}{\mathrm{D}t} = -wN^2, \tag{2.1c}$$

$$\frac{\partial u}{\partial x} + \frac{\partial w}{\partial z} = 0, \tag{2.1d}$$

where $\overline{U}$ is the mean zonal velocity with the mean shear $\overline{U}_z$ taken to be constant in this study. The linearized material derivative is $\mathrm{D}/\mathrm{D}t = (\partial/\partial t) + \overline{U}(\partial/\partial x)$; (u, w) are the perturbation velocities in the x and z directions and p is the perturbation pressure; ρ_0 is a constant reference density; $b=-(\rho/\rho_0)g$ is the perturbation buoyancy, where ρ is the density perturbation and g the gravity. The Brunt–Väisälä frequency $N^2=-(g/\rho_0)(\mathrm{d}\overline{\rho}/\mathrm{d}z)=\overline{b}_z$ is the mean vertical buoyancy gradient, where $\overline{\rho}$ is the mean density profile.

Equation set (2.1) yields, after some algebra, the vorticity equation

$$\frac{\mathrm{D}q}{\mathrm{D}t} = \frac{\partial b}{\partial x} = -\overline{b}_z \frac{\partial \zeta}{\partial x}, \tag{2.2}$$

where $q=(\partial w/\partial x)-(\partial u/\partial z)$ is (minus) the perturbation component of the vorticity perpendicular to the zonal–vertical plane and ζ is the vertical displacement. Equation (2.2) simply states that since the buoyancy is a restoring force its tendency to flatten the deformed isopycnals back generates vorticity to the right of the perturbation buoyancy gradient (figure 1; see also figure 3). By inversion, q induces a far-field vertical velocity that generates vertical displacement which, in turn, generates vorticity in the far field. To formulate this mathematically we look at a zonal Fourier component of the form of e^{ikx}, with wavenumber k, and introduce its streamfunction

https://doi.org/10.1017/S002211201000529X Published online by Cambridge University Press

$\psi(k, z)$ satisfying $u = -\partial\psi/\partial z$, $w = ik\psi$ and $q = -k^2\psi + \partial^2\psi/\partial z^2$. Then the vertical velocity at some height z can be expressed in terms of the integrated contribution of the far field vorticity field,

$$w(z) = \int_{z'} q(z')G(z, z')\,\mathrm{d}z', \tag{2.3}$$

where $G(z, z')$ is the Green function satisfying $-k^2G + (\partial^2G/\partial z^2) = ik\delta(z - z')$ with the appropriate boundary conditions. Here we apply the formulation to open flow whose perturbation vanishes at $\pm\infty$ so that $G(z, z') = -(i/2)\exp(-k|z - z'|)$. Writing then

$$\frac{\mathrm{D}\zeta}{\mathrm{D}t} = w = \int_{z'} q(z')G(z, z')\,\mathrm{d}z' \tag{2.4}$$

formulates, together with (2.2), the mathematical description for the action in a distance interaction between the buoyancy $b = -\overline{b}_z\zeta$ and the vorticity q.

The simplest non-trivial set-up of vorticity–buoyancy interaction is of a single stably stratified density jump:

$$\overline{\rho} = \rho_0 - |\Delta\overline{\rho}|H(z), \tag{2.5}$$

where $H(z)$ is the Heaviside function and the density interface is at $z = 0$. The corresponding mean buoyancy gradient is then

$$\overline{b}_z = -\frac{g}{\rho_0}\frac{\mathrm{d}\overline{\rho}}{\mathrm{d}z} = \frac{g|\Delta\overline{\rho}|}{\rho_0}\delta(z) = \Delta\overline{b}\delta(z). \tag{2.6}$$

For finite vertical displacement ζ, (2.2) implies that the vorticity perturbation should be a delta function as well, $q = \hat{q}(x, t)\delta(z)$. Equations (2.2) and (2.4) can then be written in the matrix form:

$$\frac{\partial}{\partial t}\begin{pmatrix}\hat{q}\\ \zeta\end{pmatrix} = -ik\begin{pmatrix}\overline{U}_0 & \Delta\overline{b}\\ \dfrac{1}{2k} & \overline{U}_0\end{pmatrix}\begin{pmatrix}\hat{q}\\ \zeta\end{pmatrix}, \tag{2.7}$$

where $\overline{U}_0$ is the mean velocity at $z = 0$. The solution of this simple eigenproblem is a superposition of the two Boussinesq internal gravity waves with the intrinsic phase speeds:

$$c^{\pm} = \pm\sqrt{\frac{\Delta\overline{b}}{2k}} \equiv \pm c_{gr}, \tag{2.8}$$

$$\begin{pmatrix}\hat{q}\\ \zeta\end{pmatrix} = \zeta_0^{+}\begin{pmatrix}2kc_{gr}\\ 1\end{pmatrix}\exp[-ik(c_{gr} + \overline{U}_0)t] + \zeta_0^{-}\begin{pmatrix}-2kc_{gr}\\ 1\end{pmatrix}\exp[-ik(c_{gr} + \overline{U}_0)t], \tag{2.9}$$

where $\zeta_0^{\pm}$ are the vertical displacements at $z = 0$ of the two modes. Hence, the vorticity and the vertical displacement of the eastward-propagating (westward-propagating) wave, in the mean flow frame of reference, are in phase (anti-phase), ensuring coherent propagation of the buoyancy and the vorticity fields (figure 3). Next, we use these two waves as KGW building blocks, to examine the interaction between two density jumps (see Harnik *et al.* 2008 for more details on the KGW formulation).

3. Two-density-jump instability

3.1. *Formulation*

We consider the density profile of two density jumps located at $z = \pm h$ (figure 2*a*):

$$\overline{\rho} = \rho_0 + |\Delta\overline{\rho}|[1 - H(z - h) - H(z + h)]. \tag{3.1}$$

https://doi.org/10.1017/S002211201000529X Published online by Cambridge University Press

Normalizing the length by h and the time by $1/\overline{U}_z$, (2.2) and (2.4) become

$$\left(\frac{\partial}{\partial t}+ikz\right)q=-ikRi\zeta, \tag{3.2a}$$

$$\left(\frac{\partial}{\partial t}+ikz\right)\zeta=-\frac{i}{2}\int_{z'}q(z')\exp(-k|z-z'|)\,\mathrm{d}z', \tag{3.2b}$$

where all variables are non-dimensionalized and $Ri=\overline{b}_z/(\overline{U}_z)^2$ is the Richardson number. For the two-density-jump profile

$$Ri=\frac{\Delta\overline{b}}{h(\overline{U}_z)^2}[\delta(z-1)+\delta(z+1)]\equiv\widehat{Ri}[\delta(z-1)+\delta(z+1)]. \tag{3.3}$$

The M–H condition, although commonly related to a continuously stratified flow, is obviously satisfied in this simple set-up. Taking the normalized M–H integral (cf. (4.3.3) in Baines 1998) the necessary condition to obtain non-zero imaginary phase speed requires that $\int(|\phi_z|^2+k^2|\phi|^2)\,\mathrm{d}z+\widehat{Ri}[(|\phi|^2/|z-c|^2)_{z=-1}+(|\phi|^2/|z-c|^2)_{z=1}]=(1/4)\int(|\phi|^2/|z-c|^2)\,\mathrm{d}z$, where $\phi=\psi/\sqrt{(z-c)}$. Since all the terms on the two sides of the equation are positive definite the condition can be satisfied. Nonetheless, for completeness, we analyse (in Appendix A) a continuous smooth density profile (figure 2*b*) whose limit converges to (3.1). Denoting hereafter level $z=1$ with the subscript 1 and $z=-1$ with 2 so that

$$q=\hat{q}_1\delta(z-1)+\hat{q}_2\delta(z+1), \tag{3.4}$$

we write (3.2*a*,*b*) explicitly for the two jumps:

$$\left(\frac{\partial}{\partial t}+ik\right)\hat{q}_1=-ik\widehat{Ri}\zeta_1, \tag{3.5a}$$

$$\left(\frac{\partial}{\partial t}+ik\right)\zeta_1=-\frac{i}{2}(\hat{q}_1+\hat{q}_2\,\mathrm{e}^{-2k}), \tag{3.5b}$$

$$\left(\frac{\partial}{\partial t}-ik\right)\hat{q}_2=-ik\widehat{Ri}\zeta_2, \tag{3.5c}$$

$$\left(\frac{\partial}{\partial t}-ik\right)\zeta_2=-\frac{i}{2}(\hat{q}_1\,\mathrm{e}^{-2k}+\hat{q}_2). \tag{3.5d}$$

And the intrinsic gravity wave speed in (2.8) is normalized to $c_{gr}=\sqrt{\widehat{Ri}/2k}$. By definition the two KGWs at each interface must preserve their eigenstructure of (2.9):

$$\hat{q}^{\pm}_{1/2}=\pm\sqrt{2k\widehat{Ri}}\,\zeta^{\pm}_{1/2}, \tag{3.6}$$

where, as before, the superscript $\pm$ indicates the sign of the KGW-associated intrinsic propagation speed. Since the vorticity and the displacement at each interface are superpositions of the two KGWs ($\hat{q}_{1/2}=\hat{q}^{+}_{1/2}+\hat{q}^{-}_{1/2}$, $\zeta_{1/2}=\zeta^{+}_{1/2}+\zeta^{-}_{1/2}$), (3.5*a*–*d*) can be rearranged to be written as an equation set for the KGW displacements:

$$\left[\frac{\partial}{\partial t}+ik(c_{gr}+1)\right]\zeta_1^{+}=-i\sigma\left(\zeta_2^{+}-\zeta_2^{-}\right), \tag{3.7a}$$

$$\left[\frac{\partial}{\partial t}+ik(-c_{gr}+1)\right]\zeta_1^{-}=-i\sigma\left(\zeta_2^{+}-\zeta_2^{-}\right), \tag{3.7b}$$

https://doi.org/10.1017/S002211201000529X Published online by Cambridge University Press

$$\left[\frac{\partial}{\partial t} + ik(c_{gr} - 1)\right] \zeta_2^+ = -i\sigma\left(\zeta_1^+ - \zeta_1^-\right), \tag{3.7c}$$

$$\left[\frac{\partial}{\partial t} + ik(-c_{gr} - 1)\right] \zeta_2^- = -i\sigma\left(\zeta_1^+ - \zeta_1^-\right). \tag{3.7d}$$

Equation set (3.7*a–d*) is straightforward to interpret. The mean normalized velocity at the interfaces is $\overline{U}(\pm 1) = \pm 1$; hence in the absence of interaction with the KGWs of the opposed interface (when the right-hand side are zeros), ζ_1^+ and ζ_2^- tend to propagate in the direction of the mean flow whereas ζ_1^- and ζ_2^+ propagate counter to it. Each KGW, by construction, does not interact with the other KGW of the same interface, but with the two KGWs of the opposed one. The interaction coefficient $\sigma \equiv (\mathrm{e}^{-2k}/4)\sqrt{2k\widehat{Ri}}$, results from the vorticity–displacement production relation (3.6) and the exponential evanescence of the induced vertical velocity as represented by the Green function, where the additional division by the factor 2 results from the equipartition of the vorticity at each interface between the two KGWs. The $-i$ prefix on the right-hand side indicates that the vertical velocity is induced a quarter wavelength to the right of the vorticity, recalling that for ζ^+ the vorticity and the displacement are in phase, whereas for ζ^- they are anti-phased (hence the minus sign before ζ^-; (3.6)).

3.2. *Analysis and results*

The eigenvalue solution of (3.7), for normal modes of the form of $\exp[ik(x - ct)]$, yields the dispersion relation

$$c = \pm\sqrt{c_{gr}^2 + 1 \pm 2c_{gr}\sqrt{1 + \left(\frac{\sigma}{k}\right)^2}}. \tag{3.8}$$

Without interaction ($\sigma = 0$) the solution is reduced to the four uncoupled modes: $c = \pm(c_{gr} \pm 1)$. For $\sigma \neq 0$ instability is obtained when $2c_{gr}\sqrt{1 + (\sigma/k)^2} > c_{gr}^2 + 1$. The unstable modes are stationary, $c_r = 0$, experiencing a growth rate of $kc_i = k \cdot \sqrt{-(c_{gr}^2 + 1) + 2c_{gr}\sqrt{1 + (\sigma/k)^2}}$. Figure 4(*a*) shows the growth rate as a function of $(k, \widehat{Ri})$. As can be seen a global maximum for the growth rate is obtained when $(k, \widehat{Ri}) \approx (0.5, 1)$. The wavenumber range of instability shrinks and shifts to higher wavenumbers as $\widehat{Ri}$ increases. For $\widehat{Ri}$ smaller than unity only a short-wave cutoff exists, whereas for $\widehat{Ri}$ larger than unity both short- and long-wave cutoffs exist. The unstable and stable modes come in conjugate pairs. The growth rate of these modes as well as the real phase speed of the four modes are shown for representative values of $\widehat{Ri}$ in figures 5(*a*) and 5(*b*).

The amplitude ratios and the phase differences between the four KGWs for the unstable modes (and their continuation to the neutral regions at the two sides of the cutoffs) are shown in figures 5(*c*) and 5(*d*) (normalized with respect to ζ_1^-). In the unstable region the two counter-propagating waves (ζ_1^-, ζ_2^+) have equal amplitudes. The pro-propagating waves (ζ_1^+, ζ_2^-) are also of equal amplitude, smaller by a factor χ (figure 4*b*). Each counter-propagating wave is aligned in anti-phase (in both vorticity and displacement) with the pro-propagating wave of the opposed level so that $(\zeta_1^+, \zeta_2^-) = -\chi(\zeta_2^+, \zeta_1^-)$. The two counter-propagating waves are in phase in their displacement (and anti-phased in their vorticity) at the long-wave cutoffand

https://doi.org/10.1017/S002211201000529X Published online by Cambridge University Press

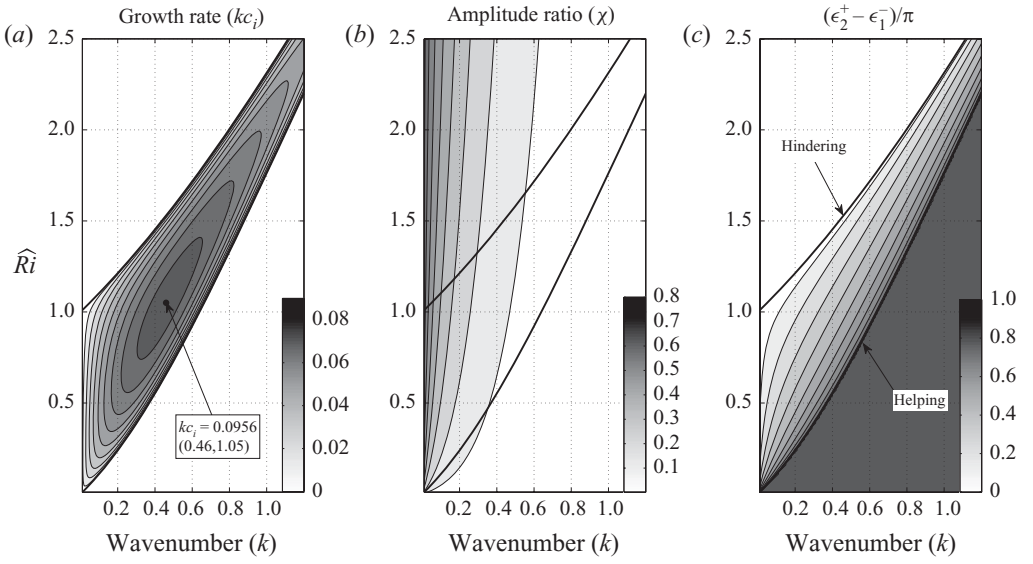


FIGURE 4. (*a*) Growth rate kc_i, (*b*) amplitude ratio (χ), $Z_1^+/Z_2^+ = Z_2^-/Z_1^-$, and (*c*) phase difference between counter-/pro-propagating waves, $\Delta\epsilon$, as functions of $\widehat{Ri}$ and k. The two black curves mark the region of instability (the boundaries of the non-zero growth rate in *a*). The global maximum in growth rate is marked in (*a*).

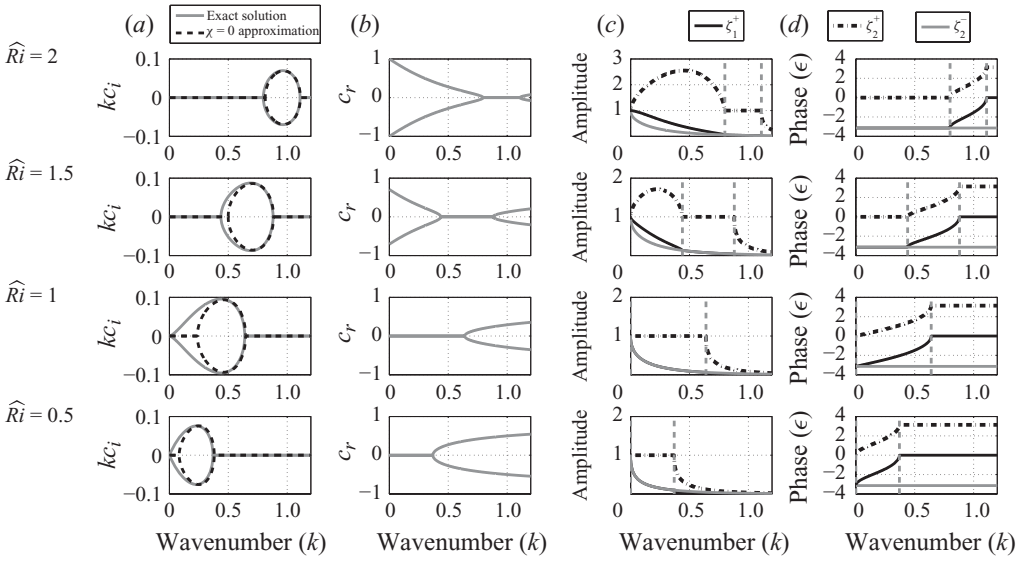


FIGURE 5. Dispersion relation and wave structure as functions of k for different values of $\widehat{Ri}$. (*a*) The growth rate (kc_i) for the exact solution with four KGWs (solid lines) and the approximate solution ($\chi = 0$) with two KGWs (dashed lines). (*b*) The real part of the phase speed for the exact solution. (*c*) The amplitude of the three kernels (for the exact solution) $\zeta_2^{\pm}$ and ζ_1^+ measured against the wave ζ_1^- which is set with $Z_1^- = 1$ and $\epsilon_1^- = 0$. (*d*) The corresponding phase of the three kernels. The values of $\widehat{Ri}$ are noted on the left side. The vertical dashed lines in (*c*) and (*d*) mark the instability region. As $\widehat{Ri}$ decreases, the range of instability shifts to smaller wavenumbers, where the ($\chi = 0$) approximation is no longer adequate.

https://doi.org/10.1017/S002211201000529X Published online by Cambridge University Press

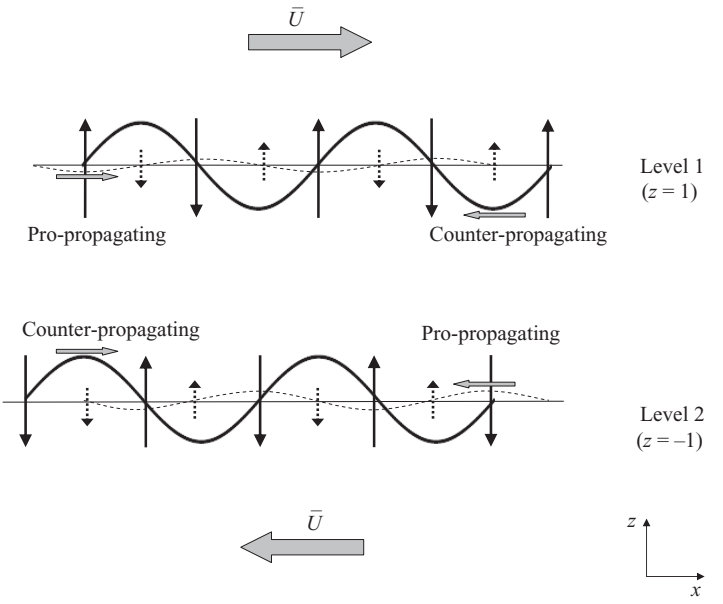


FIGURE 6. The four-KGW configuration of the most unstable normal mode of the two-density-jump problem (for which $\Delta\epsilon = \pi/2$). The displacement of the counter- and pro-propagating waves are denoted by the solid and dashed wavy lines respectively, and the corresponding kernel vertical velocity is denoted by the solid and dashed arrows respectively. Notice that both the counter- and pro-propagating pairs are mutually amplifying, and each pair hinders the other pair.

anti-phased in their displacement (and in phase in their vorticity) at the short-wave cutoff. In between, the upper counter-propagating wave displacement (vorticity) is shifted eastward (westward) with respect to the lower counter-propagating one. A schematic of the KGW set-up for the case in which the counter-propagating waves are in quadrature is drawn in figure 6. Next we wish to interpret these results from the KGW interaction point of view.

The first question that might arise is why the pro-propagating kernels are present at all in the growth mechanism. For comparison, in the analogous barotropic Rayleigh (1880) and baroclinic Eady (1949) models, only CRWs exist, and they are phase locked to yield unstable modes, similar to the counter-propagating waves (ζ_1^-, ζ_2^+) of our set-up. The reason lies in the fundamentally different action-at-a-distance mechanism between these problems. In the barotropic/baroclinic cases the induced velocity field generates vorticity at a distance by advecting the local mean (potential) vorticity gradient so that the displacement and the vorticity anomalies are either in phase or anti-phased according to the sign of the mean vorticity gradient. In our problem, the induced velocity deforms the buoyancy in the far field, while vorticity is only subsequently induced in quadrature, by the new horizontal buoyancy gradients. This initial pure buoyancy anomaly necessarily excites both KGWs. Furthermore, in order to get growth the buoyancy (or displacement) field cannot be fully in phase with or anti-phase to the vorticity field; hence they cannot be described solely by the counter-propagating kernel. To see this mathematically we write the displacement and vorticity in terms of their amplitudes and phases ($\zeta = Z\,\mathrm{e}^{i\theta}$, $q = Q\,\mathrm{e}^{i\alpha}$) and substitute a modal solution in the vorticity generation equation (2.2). Then by taking the ratio

https://doi.org/10.1017/S002211201000529X Published online by Cambridge University Press

between the imaginary and real parts of (2.2) we obtain

$$\tan(\theta-\alpha)=\frac{c_i}{c_r-\overline{U}}. \tag{3.9}$$

In our set-up $\tan(\theta-\alpha)=\mp c_i$ for levels $z=\pm 1$ so that (everywhere outside the CL) $c_i\neq 0$ is obtained only when $(\theta-\alpha)\neq(0,\pi)$. Since the pro-propagating waves must exist to obtain growth, but must also be phase locked, they must be hindered by the counter-propagating waves of the opposed level. The induced velocity by the latter on the former should be strong enough (hence the amplitude ratio χ) and of the opposite sign (hence the anti-phased alignment) to overcome the pro-propagation tendency of the former (figure 6). Since for the unstable modes $(\zeta_1^+,\zeta_2^-)=-\chi(\zeta_2^+,\zeta_1^-)$, the four KGW equations (3.7) can be reduced (without approximation) into two equations for the two counter-propagating KGWs:

$$\left[\frac{\partial}{\partial t}+ik(-\tilde{c}_{gr}+1)\right]\zeta_1^-=-i\sigma\zeta_2^+, \tag{3.10a}$$

$$\left[\frac{\partial}{\partial t}+ik(\tilde{c}_{gr}-1)\right]\zeta_2^+=i\sigma\zeta_1^-, \tag{3.10b}$$

where $\tilde{c}_{gr}=c_{gr}-\chi(\sigma/k)$ is the counter-propagating KGW intrinsic phase speed, reduced by the hindering effect of the anti-phased pro-propagating wave at the opposed boundary. Writing $\zeta_1^-=Z_1^-\,\mathrm{e}^{i\epsilon_1^-}$, $\zeta_2^+=Z_2^+\,\mathrm{e}^{i\epsilon_2^+}$ and substituting it in (3.10*a*,*b*), the real parts yield the instantaneous KGW growth rates,

$$\frac{\dot{Z}_1^-}{Z_1^-}=\frac{Z_2^+}{Z_1^-}\sigma\sin(\Delta\epsilon),\qquad \frac{\dot{Z}_2^+}{Z_2^+}=\frac{Z_1^-}{Z_2^+}\sigma\sin(\Delta\epsilon), \tag{3.11a,b}$$

while the imaginary parts yield the instantaneous KGW phase speeds,

$$c_1^-=-\frac{\dot{\epsilon}_1^-}{k}=(1-\tilde{c}_{gr})+\frac{Z_2^+}{Z_1^-}\frac{\sigma}{k}\cos\Delta\epsilon,\qquad c_2^+=-\frac{\dot{\epsilon}_2^+}{k}=-(1-\tilde{c}_{gr})-\frac{Z_1^-}{Z_2^+}\frac{\sigma}{k}\cos\Delta\epsilon, \tag{3.12a,b}$$

where $\Delta\epsilon=\epsilon_2^+-\epsilon_1^-$. For modal growth rate, $kc_i=\dot{Z}_1^-/Z_1^-=\dot{Z}_2^+/Z_2^+$; thus it is obvious that the KGWs have equal amplitudes so that $kc_i=\sigma\sin(\Delta\epsilon)$. In order for the waves to be phase locked, $c_r=c_1^-=c_2^+$, the waves should be stationary with phase locking $\Delta\epsilon$, satisfying $\cos(\Delta\epsilon)=(\tilde{c}_{gr}-1)/(\sigma/k)$. Thus, the KGW dynamics is just like the two CRWs in barotropic and baroclinic instabilities, except that the intrinsic phase speed is proportional to the square root of the wavelength (rather than the wavelength itself for the Rossby kernels) and is somewhat hindered by an opposed anti-phased kernel.

For small wavenumbers the single counter-propagation phase speed is large (2.8), and the KGWs need to be anti-phased in order to hinder each other's counter-propagation (figure 4*c*). Furthermore, the opposed pro-propagating kernel amplitude is also large (figure 4*b*) to amplify the hindering. Since the counter-propagation speed is also proportional to $\widehat{Ri}$, as it increases, such hindering can maintain phase locking only for larger wavenumbers; hence a long-wave cutoff is established for $\widehat{Ri}>1$ (figure 4*a*). As the wavenumber slightly increases, the additional hindering effect by the opposed anti-phased kernel allows the KGWs to be in a hindering–growing configuration ($0<\Delta\epsilon<\pi/2$). Ignoring this effect (by taking $\chi=0$) prevents modal growth in this range (figure 5*a*). For larger wavenumbers the amount of hindering required for phase locking is reduced, and the KGWs can be shifted towards a

https://doi.org/10.1017/S002211201000529X Published online by Cambridge University Press

more amplifying configuration, which becomes optimal when $\Delta\epsilon = \pi/2$ (figure 6). This occurs for wavenumbers and Richardson numbers that satisfy $\tilde{c}_{gr} = 1$, which is when each KGW (with its anti-phased opposed one) counter-propagates with a speed which balances exactly the mean flow speed. For even larger wavenumbers the counter-propagation speed is overwhelmed by the mean flow, and the KGWs need to be in a helping–growing configuration ($\pi/2 < \Delta\epsilon < \pi$). In this range the hindering effect of the pro-propagating waves interferes with the phase locking, and therefore χ decreases (figure 4*b*). Eventually the wavenumber becomes too large for effective phase locking (because both the counter-propagation speed and the interaction coefficient σ decrease with the wavenumber), and a short-wave cutoff is established. Increasing the Richardson number increases the counter-propagation speed and hence shifts both the long- and short-wave cutoffs to higher wavenumbers but also shrinks the transition between them.

Summarizing this part of the analysis, we examine in detail the action-at-a-distance paradigm of Baines & Mitsudera (1994) to stratified shear flow instability, in the simplest model we could construct. This model shares many similarities with the baroclinic Eady (1949) and barotropic Rayleigh (1880) models, but is fundamentally different in the sense that it does not satisfy the Rayleigh–Fjørtoft conditions for instability and that each interface supports two edge waves rather than one. Although the dynamics is more complex, the essence of the instability is the same – it is dominated by the phase-locked constructive interaction between the two counter-propagating interfacial waves (IWs).

These three models, however, do not contain a CL (they do contain a steering level in the middle, where $\overline{U} = c_r$, but the vorticity perturbation is zero there). Therefore, in the next section we proceed by adding a small ambient stratification to the two density jumps (figure 3*c*), to examine the effect of the CL on the instability from the vorticity–buoyancy action-at-a-distance perspective.

4. Suppression of instability by ambient stratification

4.1. *Results*

We consider the density profile of figure 3(*c*):

$$\overline{\rho} = \rho_0 + |\Delta\overline{\rho}|[1 - H(z-h) - H(z+h)] - z|\overline{\rho}_z|_{amb} \tag{4.1}$$

($|\overline{\rho}_z|_{amb} = \text{constant}$), where the ambient Richardson number (outside the jumps) satisfies $0 < Ri_{amb} = -[(g/\rho_0)|\overline{\rho}_z|_{amb}]/(\overline{U}_z)^2 < 1/4$ so that

$$Ri(z) = Ri_{amb} + \widehat{Ri}[\delta(z-1) + \delta(z+1)]. \tag{4.2}$$

We find the normal-mode solutions of this set-up both by numerical discretization of (2.2) and (2.4) (Appendix B) and by converting them to the Taylor–Goldstein equation and solving it analytically (Appendix C). The agreement between the two methods of solution is excellent (the two solutions for $\widehat{Ri} = 2$, $Ri_{amb} = 0.2$ and $k = 1.07$ differ at most by 0.46 %). As in the previous set-up four discrete normal modes exist, for each zonal wavenumber, where the growing and decaying modes (if they exist) come in conjugate pairs.

Figure 7 shows the dispersion relation for the growing and decaying modes as Ri_{amb} increases gradually from 0 to 1/4. We choose to show the case in which $\widehat{Ri} = 2$, since in the absence of ambient stratification the dispersion relation includes a distinct long-wave cutoff, and the role of the pro-propagating IWs is negligible (cf.

https://doi.org/10.1017/S0022112010005290X Published online by Cambridge University Press

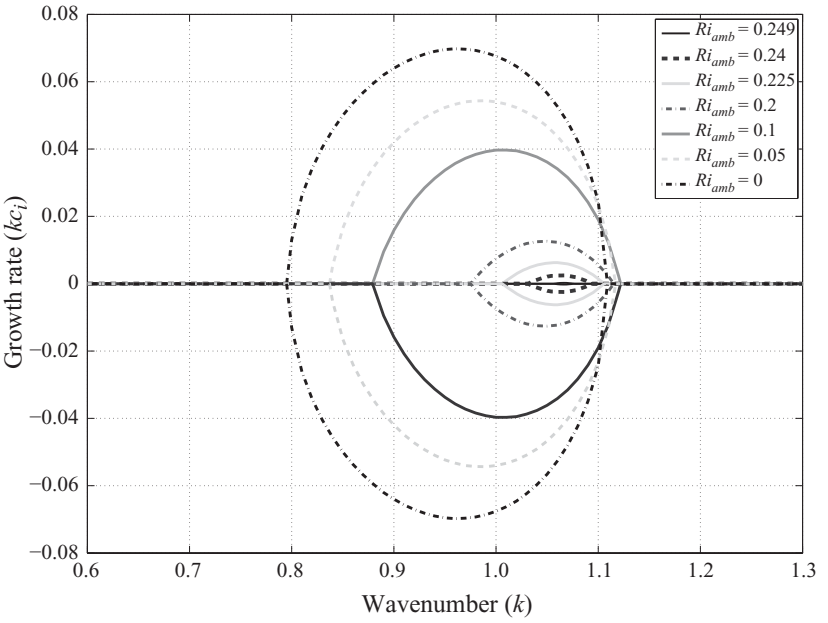


FIGURE 7. The growth rate (kc_i) as a function of wavenumber (k) for different values of Ri_{amb} given in the figure legend, with the outermost curve corresponding to $Ri_{amb} = 0$ and the innermost curve to $Ri_{amb} = 0.249$. For all wavenumbers in the unstable zone there are two complex-conjugate phase speeds $c = \pm ic_i$. The real part of the phase speed for the unstable modes is zero in all cases.

the topmost row of figure 5; the pro-propagating IWs were found to be unessential to the dynamics with ambient stratification). As Ri_{amb} increases the growth rate decreases, and the spectrum emitting the instability shrinks and is shifted towards higher wavenumbers. As expected from the M–H criterion the instability ceases when the Richardson number becomes larger than a quarter everywhere in the flow. In figure 8 we show the structure of the amplitudes and phases of the vorticity and the vertical displacements, for a specific wavenumber ($k = 1.07$) and for various values of Ri_{amb}. The IWs hardly change with Ri_{amb}; the vorticity IWs remain tilted against the shear, by approximately a quarter of wavelength, and the displacement of the lower (upper) IW is almost in phase (anti-phase) with its vorticity. Although the ambient stratification is constant everywhere in the domain the vorticity and the displacement are concentrated at the critical layer whose width decreases as the value of Ri_{amb} approaches a quarter (e.g. figure 8).

4.2. *Interfacial-wave–critical-layer far-field interaction*

This structure, which is drawn for $Ri_{amb} = 0.249$ in figure 9, can be understood from the vorticity–buoyancy view when considering first the vertical displacement profile in the absence of ambient stratification. Although the vertical velocity resulting from the combined induction of the two IWs is minimized at the CL (because of the evanescence of the Green function), the vertical displacement is maximized there. This is because the fluid at the CL is phase locked with the two IWs, and therefore its vertical displacement is amplified persistently ((2.4) yields that $\zeta = w/[ik(\overline{U} - c_r) + kc_i] = w/kc_i$ at the CL) and tends to infinity as c_i goes to zero. In the presence of ambient stratification the vertical displacement at the CL deforms the isopycnal surfaces and hence generates strong vorticity a quarter wavelength

https://doi.org/10.1017/S002211201000529X Published online by Cambridge University Press

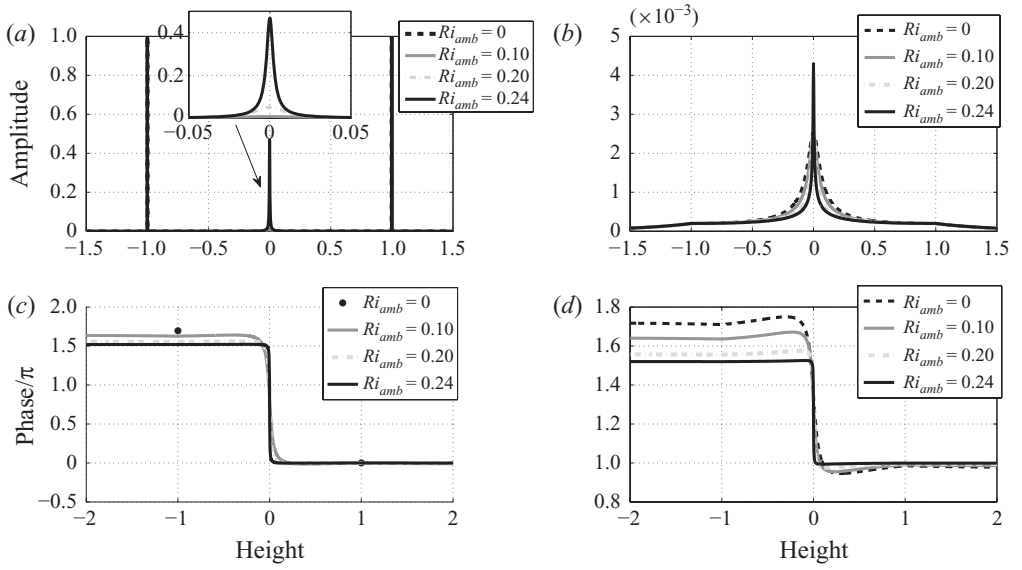


FIGURE 8. (*a,b*) Amplitude and (*c,d*) phase of (*a,c*) the vorticity and (*b,d*) the displacement as functions of height for parameter values $\widehat{Ri} = 2$ and $k = 1.07$ and varying Ri_{amb} shown in the figure legend. Values are normalized so that the maximum amplitude is 1 and the vorticity phase is 0 at $z = 1$. Note that all q amplitude curves (*a*) lie on top of each other at the jumps, and for $Ri_{amb} = 0$ the vorticity is zero except at the jumps; thus its phase is marked as dots in (*c*). In the critical layer, when $Ri_{amb} > 0$, the amplitudes are increased, and a rapid transition of the phase occurs. Away from the critical layer, q and ζ are approximately in two regions of equal phase.

to its right in a standing-wave-like fashion ($q = i(Ri_{amb}/c_i)\zeta$; (2.2) and figure 9; cf. Appendix B in Harnik *et al.* 2008).

Adding a small background stratification thus adds a third active region to the two-jump dynamics. It would simplify things, conceptually, to represent the CL region as a single standing-wave kernel with a structure at the exact centre of the CL (q and ζ in quadrature in both space and time; cf. Appendix B of Harnik *et al.* 2008). Such a vorticity kernel induces an evanescent untilted vertical velocity field. This representation is valid, since the far-field vertical velocity induced by the entire CL (the region in which q and ζ are strongly phase tilted with height) is indeed evanescent and almost untilted (a tilt of 0.012π for $Ri_{amb} = 0.225$ and less than 0.0005π for $Ri_{amb} = 0.249$). The reason that the CL region affects the flow like a single kernel at its centre is partly due to the strong vorticity amplitude decay away from the CL centre and partly due to the strong vorticity phase tilting which causes the top and bottom parts of the CL to largely cancel each other's influence at a distance.

Looking at a schematic illustration of a three-kernel representation of the configuration of figure 9, drawn in figure 10, it is clear that if the induced vertical velocity field from the two kernels is shifted by a quarter wavelength, symmetry yields that the maximum induced displacement at the CL should be one eighth wavelength in between the two IWs. Then the vorticity anomaly at the CL, generated in quadrature in response to the induced displacement, induces a vertical velocity anomaly, which tends to oppose the existing displacement anomaly at all levels. Since this CL-induced vertical velocity is not exactly in anti-phase with the IW displacements, it also tends

https://doi.org/10.1017/S002211201000529X Published online by Cambridge University Press

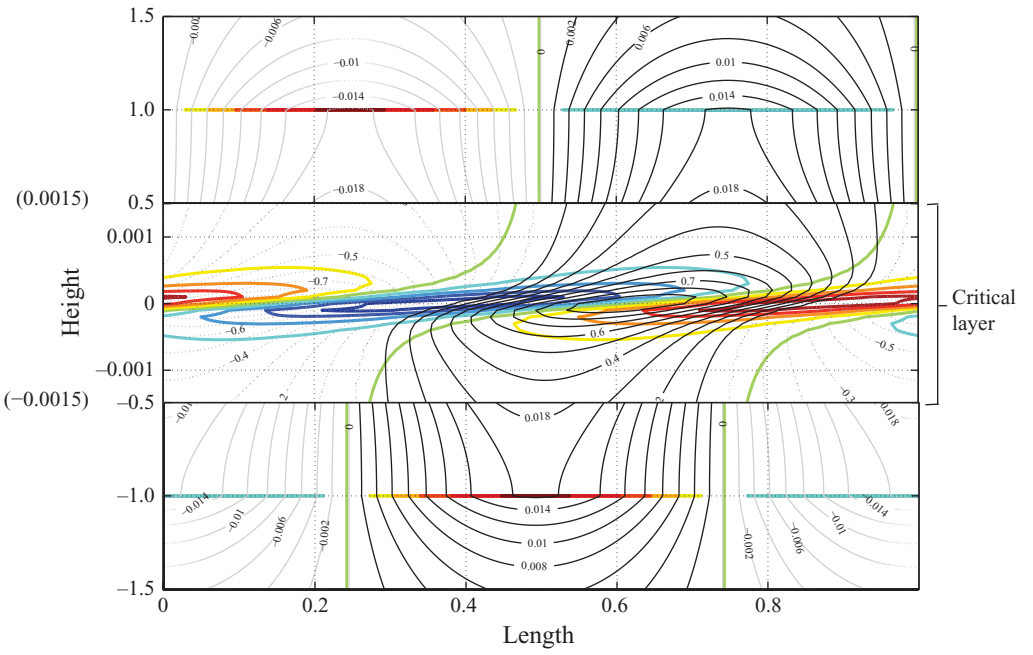


FIGURE 9. The x–z contour plots of the vorticity and the displacement for $k = 1.07$ and $Ri_{amb} = 0.249$. The colour contours show q with the positive values in red and yellow and the negative values in blue and green. The black contours show ζ, where the lighter shades are the negative values and the darker shades are the positive values. The normalized q contour interval is 0.2, and the normalized ζ values are marked on the plot. The CL is enlarged and overlain on the centre so that the height axis is discontinuous at $z = \pm 0.5$. The length is given in units of wavelength.

to shift the IW in the direction of the shear (a hindering effect). Moreover, the CL-induced displacement anomaly also acts to decrease its own amplitude growth in a standing-wave-like fashion.

As Ri_{amb} approaches a quarter, the vorticity at the CL approaches infinity, and its induced destructive velocity completely masks the constructive interference between the two IW vorticity delta functions. This argument is somewhat circular for normal modes, since as the growth rate goes to zero, (2.2) indicates that the CL vorticity goes to infinity; therefore it is difficult to differ between cause and effect. For this reason we simulate the evolution towards the normal modes from various initial conditions, including beginning from the phase-locked IWs with zero ambient vorticity. The simulations (not shown here) indicate indeed that the CL is the region which is persistently amplified by the IWs, and as the CL vorticity grows it acts to dampen the IWs. The unstable mode which last survives is that for which the IWs are in the optimal constructive interference phase of $\pi/2$ (which is of wavenumber $k = 1.07$, shown in figures 8–10). As Ri_{amb} crosses a quarter all modes become neutral. This schematic picture is slightly altered by the integrated effect of the non-zero vorticity kernels outside the CL and the interfaces. These kernels are in phase with their adjacent interfaces (figure 8) and therefore act to help them to counter-propagate against the shear. This effect overwhelms the opposed hindering by the CL, and consequently the unstable regime is shifted towards the helping regime in the dispersion relation as Ri_{amb} increases (figure 7). The other difference is that when $Ri_{amb} < 1/4$ the CL is

https://doi.org/10.1017/S002211201000529X Published online by Cambridge University Press

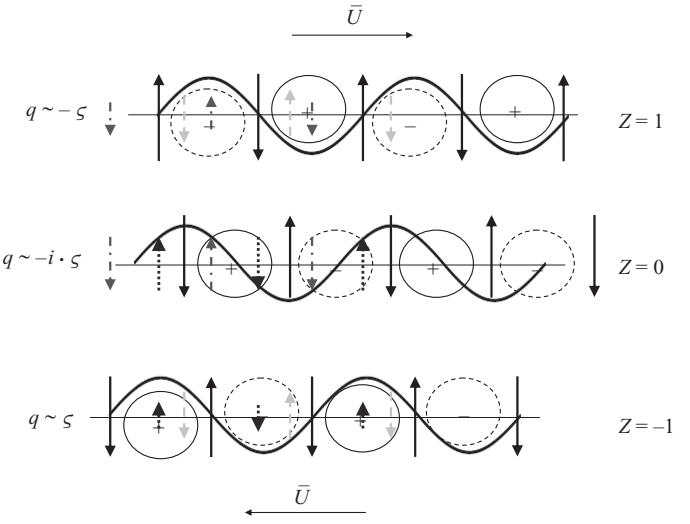


FIGURE 10. The three-wave mechanism for the most unstable wavenumber resulting in a $\pi/2$ phase difference between the interfacial kernels' displacement. The wavy lines illustrate the displacement, and the circles show the vorticity with the anomaly sign marked and the negative circles dashed. The large arrows represent the self-vertical velocity generated by the local wave, while the small dashed or dotted arrows are the induced vertical velocity generated by the two other levels. The IWs ($z = \pm 1$) are pure ζ^- and ζ^+ kernels respectively as in the two-density-jump model. The CL wave ($z = 0$) consists of q and ζ anomalies which are $\pi/2$ out of phase and a displacement phase difference of $\pi/4$ from the IWs so that it is situated in equal spacing from both.

actually a layer with a finite width (figure 9). Nonetheless its overall effect remains destructive.

4.3. *Energy and momentum flux consideration*

The destructive role of the CL seems surprising in light of the fact that this is a place where energy is extracted from the mean flow to the perturbation (Lindzen & Tung 1978). For the barotropic/baroclinic case Harnik & Heifetz (2007) showed that the CRW kernels, adjacent to the CL, are governed by the action-at-a-distance from remote dominating kernels. Next we show that this is also the case for the stably stratified shear set-up. Lindzen & Tung (1978) and Lindzen & Barker (1985) looked at the energy flux carried by propagating waves (across the shear) at the vicinity of the CL and found that energy flux diverges at the CL when over-reflection occurs. To inspect the energy flux they applied the first theorem of Eliassen & Palm (1960) (strictly valid for steady flow, but has been shown to be a good approximation for small growth rate instability as well):

$$\overline{pw} = -\rho_0(\overline{U} - c)\overline{uw} \tag{4.3}$$

(where the bar denotes zonal averaging). For positive shear, energy flux divergence ($\overline{pw} > 0$ above the CL and $\overline{pw} < 0$ below it) is obtained when the momentum flux $\overline{uw} < 0$ at both its sides (and thus the energy growth $-\overline{uw}U_z$ is positive there). This view of the CL and energy extraction from the mean flow arises naturally in the over-reflection view of things. Here we view this energy flux divergence at the CL through our kernel action-at-a-distance approach to gain further insight into the relative

https://doi.org/10.1017/S002211201000529X Published online by Cambridge University Press

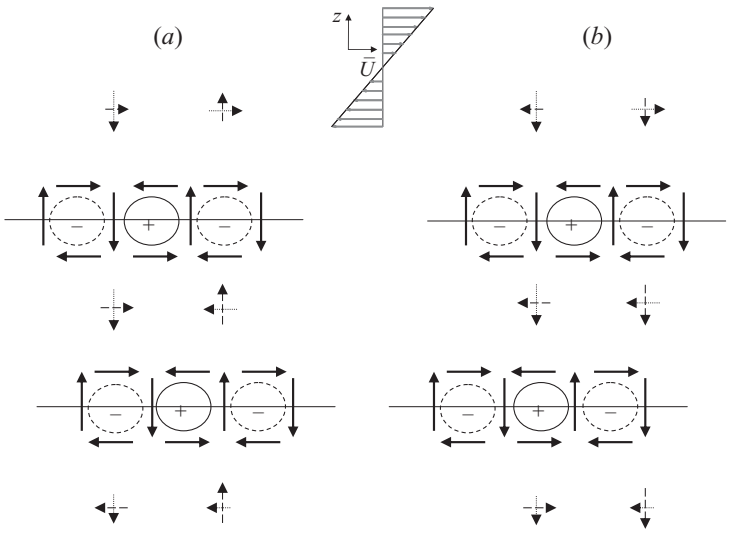


FIGURE 11. The momentum flux ($\overline{uw}$) induced by two vorticity anomalies: (*a*) tilted against the shear and (*b*) tilted with the shear with a phase difference of $\pi/2$. The thick arrows are the local velocities (vertical and horizontal), while the dotted and dashed arrows are the induced velocities by the upper and lower (respectively) perturbations. In between the two anomalies $\overline{uw}$ is negative for (*a*) and positive for (*b*). Notice that for both (*a*) and (*b*), above the top anomaly and below the bottom one the two contributions to $\overline{uw}$ are of equal magnitude and opposite signs, resulting in a zero total momentum flux.

contribution of the CL and IWs. Towards this end we first develop an understanding of the kernel action-at-a-distance contribution to the momentum flux $\overline{uw}$.

By definition, the zonal and vertical velocities induced by a single kernel are in quadrature and therefore do not contribute to the momentum flux $\overline{uw}$. Therefore, from the KGW perspective, the momentum flux is inherently non-local, as it results from the interaction between different kernels. If we denote the contribution to the momentum flux at some level z, from two kernels located at z' and z'', as $[\overline{uw(z', z'')}]_z$, then if z is sandwiched between the kernels, i.e. $z'' > z > z'$, figure 11 indicates that the momentum flux is negative (positive) when the kernels' vorticity is tilted westward (eastward) with height. Furthermore, the kernels' contributions are even in the sense that $[\overline{uw(z', z'')}]_z = [\overline{u(z')w(z'')}]_z + [\overline{u(z'')w(z')}]_z = 2[\overline{u(z')w(z'')}]_z$. Moreover $[\overline{uw(z', z'')}]$ is independent of height everywhere between the two kernels (if z, for instance, is closer to the upper kernel, from below the weaker contribution from the lower kernel is compensated by the stronger contribution from the upper one). In contrast, outside the kernels ($z > z''$ or $z < z'$) the contribution vanishes since $[\overline{u(z')w(z'')}]_z = -[\overline{u(z'')w(z')}]_z$.

Applying the cases of figure 11 to our problem, as presented for example in figures 8–10, it is clear that the interaction between the two IWs (tilted westward, against the shear) yields a negative contribution to $\overline{uw}$ in between them and hence a positive contribution to the energy growth. Thus, the mutual amplification between the two kernels can also be expressed by a positive contribution to the energy flux divergence at the CL. The kernel at the CL is tilted with the shear relative to both IWs, and therefore the interaction between the IWs and the CL contributes towards positive $\overline{uw}$ and hence towards energy flux convergence at the CL. Furthermore, since the vorticity at the CL (having a small finite width) is tilted with the shear it contributes towards a positive momentum flux.

https://doi.org/10.1017/S002211201000529X Published online by Cambridge University Press

In Appendix D we derive the overall integrated expression for the momentum flux, evaluated at height z, in terms of kernels' interaction (at height z' and z'') to be

$$-[\overline{uw}]_z = \frac{1}{4}\int_{z'=-\infty}^{z}\int_{z''=z}^{\infty} Q(z')Q(z'')\sin[\alpha(z'')-\alpha(z')]\exp[-k(z''-z')]\,\mathrm{d}z'\,\mathrm{d}z''. \quad (4.4)$$

As a quantitative example we compute $\overline{uw}$, for the solution $k=1.07$ and $Ri_{amb}=0.24$, at $z=0$. For this case the CL is concentrated at $|z|<\delta\approx 0.002$ (figure 8). Above and below δ the vorticity structure is almost untilted and in phase with its associated IW. Hence we can decompose the double integral of (4.4) into three contributions: (i) $\int_{z'=-\infty}^{-\delta}\int_{z''=\delta}^{\infty}$, accounting for the constructive interaction between the kernels outside the CL; this interaction is dominated by the two-IW interaction; (ii) $\int_{z'=-\infty}^{-\delta}\int_{z''=0}^{\delta} + \int_{z'=-\delta}^{0}\int_{z''=\delta}^{\infty}$, accounting for the destructive interaction between the CL and the kernels outside of it; this interaction is dominated by the destructive interaction between the CL and the IWs; (iii) $\int_{z'=-\delta}^{0}\int_{z''=0}^{\delta}$, accounting for the destructive interaction between the kernels within the CL. Normalizing the whole contribution of (4.4) at $z=0$ to unity,

$$-\overline{uw}(z=0)=1=\text{(i)}+\text{(ii)}+\text{(iii)}=49.2-32.1-16.1. \quad (4.5)$$

Hence the dominated IW–IW positive contribution is almost balanced by both the IW-CL interaction and the self-destructive effect of the CL kernels. Indeed the mode is only slightly unstable.

5. Summary and discussion

The dynamics of linear shear flow can be examined from a wave theory perspective or alternatively from a field theory one. These two perspectives are very different from each other. The former views the dynamics in terms of the ability of waves to propagate/decay/become absorbed/become reflected or over-reflected, in different regions across the shear. The latter views the dynamics in terms of instantaneous action-at-a-distance interaction across the shear, between different remote vorticity waves propagating against the shear (but not across it). Each of the perspectives is valid, of course, and preferring one to the other is in some sense a matter of personal taste. For barotropic and baroclinic instabilities large bodies of literature exist for the two perspectives, and recently Harnik & Heifetz (2007) related them to obtain a deeper understanding of the instability mechanism. For stratified shear flows, however, most of the research literature takes the wave theory point of view. The current study continues the work of Baines & Mitsudera (1994) and Harnik *et al.* (2008) in an attempt to establish a coherent field theory perspective to stratified shear flow instability.

The need for such a perspective arises because the basic intuition associated with the M–H criterion – that the shear acts to destabilize the flow, while the stratification acts to stabilize it – fails when considering a simple set-up of a Boussinesq plane Couette flow with two density jumps. Without the jumps the flow is sheared and unstratified; yet it is neutral with respect to modal perturbations. Counter-intuitively, it is destabilized when stable stratification is added. (This effect was actually manifested earlier by Lindzen & Barker 1985, who showed that two stably stratified regions are needed to extract energy from a Couette flow.) This set-up is analogous in some aspects to the baroclinic Eady (1949) model. There the over-reflection view (wave theory) seems a bit artificial, while the Rossby edge wave interaction view (field theory) seems more natural. Nevertheless, the over-reflection

https://doi.org/10.1017/S002211201000529X Published online by Cambridge University Press

approach has been under investigation more intensely and therefore covers many cases such as viscous flow (Lindzen & Rambaldi 1986) and normal-mode as well as non-modal instabilities (Lindzen & Rosenthal 1981). Non-normal-mode instability has only been fairly recently interpreted by the field perspective (Heifetz & Methven 2005).

As opposed to the Eady (1949) model, where the Rossby IWs are generated by potential vorticity gradients, here the vorticity IWs are gravity waves generated by buoyancy gradients. In the Eady model each interface supports one CRW, whereas here two gravity waves exist at each density jump, one counter-propagating and one pro-propagating with the mean flow. Although this complicates the dynamics and although the wave generation mechanism is different, we have shown in detail that the essence of the instability is the same as in the Eady model. The two counter-propagating waves, one from each interface, dominate the dynamics as they phase lock each other in a growing configuration. The role of the pro-propagating waves was found to be minor (mainly in expanding the spectral range of instability in the low-wavenumber hindering regime). These results are in line with the view of Baines & Mitsudera (1994).

This simple set-up by itself emphasizes the subtleties associated with the M–H criterion. A single density jump in a plane Boussinesq Couette flow satisfies the M–H necessary, but insufficient, condition for instability (since the Richardson number is a delta function there and zero elsewhere); nonetheless the flow is neutral. Only when another density jump is added so that gravity waves can interact constructively at a distance, the flow becomes unstable. Furthermore, it seems strange that if we add an ambient stratification in between the density jumps so that the ambient Richardson number exceeds the small value of a quarter (compared with infinity in the two jumps), the instability is shut down. The explanation of Baines & Mitsudera (1994), that the waves are then absorbed by the CL and hence are heavily damped, mixes arguments from the two perspectives. Here we used the field theory KGW formulation derived by Harnik *et al.* (2008), which can be applied to continuous stratification as well, to show that the CL is the region which is persistently amplified by the IWs, simply because fluid parcels there have no relative zonal motion with respect to the locked IWs. Hence, although the ambient stratification is small and uniform everywhere, at the CL the particle displacement anomalies are large so that the resulting buoyancy generation of vorticity is also large. The resulting continuous dynamical structure can be then simplified to a three-kernel dynamics – two counter-propagating IWs at the interfaces and one standing-wave kernel at the CL.

From this perspective, the CL does not 'absorb' the two interacting waves; rather it is a standing-wave-like kernel which decreases the two mutually amplifying kernels. This instability is allowed only when the CL effect is weak enough, that is, when the Richardson number is smaller than a quarter. This destructive role of the CL may seem surprising, when recalling that in the CL energy flux is diverging; hence energy is being yanked from the mean flow to the perturbation. The kernel formulation provides a rigorous way to compute the action-at-a-distance contribution of the remote kernels to the energy flux. It then turns out that it is the interaction between the two IWs that contributes towards positive energy flux divergence at the CL, while the interaction between the CL kernel and the IWs contributes towards energy flux convergence and therefore towards stabilization of the flow (a similar effect has been observed by Harnik & Heifetz 2007 in barotropic and baroclinic shear flows).

To conclude, we investigated one of the simplest set-ups for stably stratified shear flow instability, and still the physical mechanism of the instability is far from being

https://doi.org/10.1017/S002211201000529X Published online by Cambridge University Press

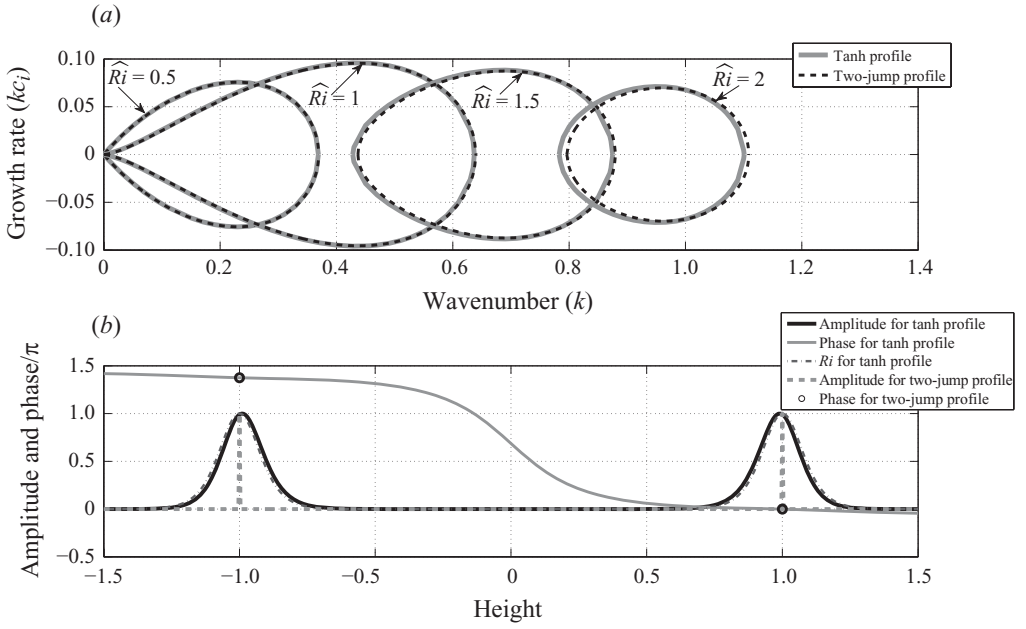


FIGURE 12. The continuous 'tanh' density profile solution in comparison with the two-density-jump solution for (*a*) the growth rate as a function of the wavenumber and (*b*) the amplitude and phase for the most unstable wavenumber in the case of $\widehat{Ri} = 1$. The tanh solution converges to the two-density-jump solution when $\epsilon \to 0$. In (*a*), $\epsilon = 0.01$ was chosen, while for (*b*), $\epsilon = 0.1$, since the former value produces indistinguishable amplitude solutions (the vorticity amplitude for the tanh solution appears to be two delta functions).

simple. A possible reason for this is that the M–H theorem is necessarily spectral (one must assume *a priori* a modal solution to obtain the condition) and hence is not derivable from Hamiltonian considerations (Shepherd 1990). This stands in contrast to barotropic and baroclinic shear flows whose instability conditions can be derived from globally conserved Hamiltonians (Heifetz, Harnik & Tamarin 2009).

We are grateful to the Israeli Science Foundation (1084/06 and 1370/08).

Appendix A. Two density jumps as a limit case of a continuous density profile

The continuous density profile (figure 2*b*)

$$\overline{\rho} = \rho_0 - \frac{|\Delta\overline{\rho}|}{2}\left[\tanh\frac{z-h}{\epsilon h} + \tanh\frac{z+h}{\epsilon h}\right] \tag{A 1}$$

yields the Richardson number

$$Ri = \frac{\widehat{Ri}}{2\epsilon}[2 - (\tanh^2((z-1)/\epsilon) + \tanh^2((z+1)/\epsilon))], \tag{A 2}$$

where $\epsilon > 0$ is a tunable parameter measuring the relative width of the layer (in which the density varies) compared with the distance between the layers. When $\epsilon \to 0$, (A 1) and (A 2) converge respectively to (3.1) and (3.3). It is straightforward to show that the M–H criterion is satisfied for this continuous profile. In figure 12

https://doi.org/10.1017/S002211201000529X Published online by Cambridge University Press

we take $\epsilon = 0.01$ and solve the eigenvalue problem, both by the kernel approach to the vorticity–displacement equations (Appendix B) and by a shooting method of the Taylor–Goldstein equation. Figure 12(*a*) shows the growth rate solution for various values of $\widehat{Ri}$. The agreement with the discontinuous solution (figure 5*a*) is excellent. Figure 12(*b*) shows the profile of the Richardson number for $\widehat{Ri} = 1$ and the vorticity structure of its most unstable mode ($k = 0.43$). The vorticity is maximized at $z = \pm 1$, and the phase difference between these two points ($\epsilon \approx 1.4\pi$) is in perfect agreement with the discontinuous profile (the plots second from the bottom in figure 5*c*,*d*).

Appendix B. Numerical modal solution of the vorticity–displacement equations

Discretizing the normalized version of (2.2) and (2.4) yields

$$\left(\frac{\partial}{\partial t} + ikz_j\right) q_j = -ikRi_j\zeta_j, \tag{B 1}$$

$$\left(\frac{\partial}{\partial t} + ikz_j\right) \zeta_j = \sum_{n=1}^{N} q_n G_{j,n}. \tag{B 2}$$

The domain is taken between $(-3.5, 3.5)$ to assure no numerical boundary effect (the density jumps are located at $z = \pm 1$). Furthermore, $N = (7/\Delta z) + 1 = 1751$ is the number of points at which sufficient accuracy is obtained for $\Delta z = 4 \times 10^{-3}$. The Richardson number profile of (4.2) is discretized so that $Ri(z = \pm 1) = \widehat{Ri}/\Delta z$ and $Ri(z \neq \pm 1) = Ri_{amb}$ elsewhere. The discretized Green function is $G_{j,n} = -\Delta z \cdot (i/2)\exp(-k|z_j - z_n|)$. Redefining $\tilde{G} = (i/k)G$, (B 1) and (B 2) can be written in the matrix form:

$$\frac{\partial}{\partial t}\begin{pmatrix} q_1 \\ \cdot \\ \cdot \\ q_N \\ \zeta_1 \\ \cdot \\ \cdot \\ \zeta_N \end{pmatrix}_{2N\times 1} = -ik \cdot \underbrace{\begin{pmatrix} z_1 & 0 & \cdot & 0 & Ri_1 & 0 & \cdot & 0 \\ 0 & \cdot & & \cdot & 0 & \cdot & & \cdot \\ \cdot & & \cdot & 0 & \cdot & & \cdot & 0 \\ 0 & \cdot & 0 & z_N & 0 & \cdot & 0 & Ri_N \\ \tilde{G}_{1,1} & \cdot & \cdot & \tilde{G}_{1,N} & z_1 & 0 & \cdot & 0 \\ \cdot & \cdot & & \cdot & 0 & \cdot & & \cdot \\ \cdot & & \cdot & \cdot & \cdot & & \cdot & 0 \\ \tilde{G}_{N,1} & \cdot & \cdot & \tilde{G}_{N,N} & 0 & \cdot & 0 & z_N \end{pmatrix}}_{\mathrm{A}_{2N\times 2N}} \begin{pmatrix} q_1 \\ \cdot \\ \cdot \\ q_N \\ \zeta_1 \\ \cdot \\ \cdot \\ \zeta_N \end{pmatrix}_{2N\times 1}, \tag{B 3}$$

where the normal modes are the eigensolution of (B 3).

Appendix C. Analytical solution of Taylor–Goldstein equation

Applying the linearized material derivative $\mathrm{D}/\mathrm{D}t$ to the normalized version of (2.2), expressing the vorticity and the vertical velocity in terms of the streamfunction and looking for the normal-mode solution yield the Taylor–Goldstein equation (e.g. Baines 1998) with zero shear curvature:

$$\psi_{zz} + \left[\frac{Ri}{(z-c)^2} - k^2\right]\psi = 0. \tag{C 1}$$

https://doi.org/10.1017/S002211201000529X Published online by Cambridge University Press

For the transformation of variables $y=(z-c)k$ and $\widetilde{\psi}=\psi/\sqrt{y}$, the Taylor–Goldstein equation is transformed into the modified Bessel equation (e.g. Sneddon 1956)

$$y^2\widetilde{\psi}_{yy}+y\widetilde{\psi}_y-(y^2+\nu^2)\widetilde{\psi}=0, \tag{C 2}$$

with $\nu=\sqrt{1/4-Ri}$, whose general solution is

$$\psi=\sqrt{y}[C_1I_\nu(y)+C_2I_{-\nu}(y)], \tag{C 3}$$

where I_ν and $I_{-\nu}$ are the modified Bessel functions and C_1 and C_2 are two constants. Equivalently we can obtain the Bessel function from the Taylor–Goldstein equation by writing $\widetilde{y}=iy$,

$$\widetilde{y}^2\widetilde{\psi}_{\widetilde{y}\widetilde{y}}+\widetilde{y}\widetilde{\psi}_{\widetilde{y}}+(\widetilde{y}^2-\nu^2)\widetilde{\psi}=0, \tag{C 4}$$

whose solution is

$$\psi=\sqrt{y}[AH_1(iy)+BH_2(iy)], \tag{C 5}$$

where H_1 and H_2 are the Hankel functions and A and B are two constants. Since the two formulations are equivalent we arbitrarily choose to use the Hankel functions for the matching solution.

We hence decompose the set-up of figure 2(c) into the three domains, namely (i) $z>1$, (ii) $-1<z<1$ and (iii) $z<-1$, and look for the solution $\psi_j=\sqrt{y}[A_jH_1(iy)+B_jH_2(iy)]$, where the subscript $j=1,2,3$ indicates the domain. We require continuity of the streamfunction:

$$z=1:\ \psi_1=\psi_2;\qquad z=-1:\ \psi_2=\psi_3. \tag{C 6a,b}$$

Integration of the vorticity across $z=1$ together with the definition (3.4) of the vorticity there yields

$$\left[\frac{\partial\psi_1}{\partial z}-\frac{\partial\psi_2}{\partial z}\right]_{z=1}=\hat{q}_1. \tag{C 7}$$

The Taylor–Goldstein equation then suggests that

$$\left[\frac{\partial\psi_1}{\partial z}-\frac{\partial\psi_2}{\partial z}=-\frac{\widehat{Ri}}{(1-c)^2}\psi\right]_{z=1}, \tag{C 8}$$

and similarly for $z=-1$ we obtain

$$\left[\frac{\partial\psi_2}{\partial z}-\frac{\partial\psi_3}{\partial z}=-\frac{\widehat{Ri}}{(1-c)^2}\psi\right]_{z=-1}. \tag{C 9}$$

The outer radiation conditions of $\psi_1(z\to\infty)=0$ and $\psi_3(z\to-\infty)=0$ set $B_1=A_3=0$. Substituting (C 5) into (C 6), (C 8) and (C 9) and writing $y_1=k(1-c)$ and $y_2=k(-1-c)$ we get

$$A_1H_1(iy_1)=A_2H_1(iy_1)+B_2H_2(iy_1),\quad A_2H_1(iy_2)+B_2H_2(iy_2)=B_3H_2(iy_2), \tag{C 10a,b}$$

$$(A_1-A_2)\left[\frac{\partial}{\partial z}[\sqrt{y}H_1(iy)]_{y_1}\right]-B_2\left[\frac{\partial}{\partial z}[\sqrt{y}H_2(iy)]_{y_1}\right]-A_1\frac{\widehat{Ri}}{(1-c)^2}\sqrt{y_1}H_1(iy_1)=0, \tag{C 11}$$

$$(B_2-B_3)\left[\frac{\partial}{\partial z}[\sqrt{y}H_2(iy)]_{y_2}\right]+A_2\left[\frac{\partial}{\partial z}[\sqrt{y}H_1(iy)]_{y_2}\right]-B_3\frac{\widehat{Ri}}{(1-c)^2}\sqrt{y_2}H_2(iy_2)=0. \tag{C 12}$$

https://doi.org/10.1017/S002211201000529X Published online by Cambridge University Press

Hence, in order to obtain a non-trivial solution, $\mathrm{Det}(M)=0$, where

$$M=\begin{pmatrix} H_1(iy_1) & -H_1(iy_1) & -H_2(iy_1) & 0 \\ \dfrac{\partial}{\partial z}[\sqrt{y}H_1(iy)]_{y_1}+\dfrac{\widehat{Ri}}{(1-c)^2}\sqrt{y_1}H_1(iy_1) & -\dfrac{\partial}{\partial z}[\sqrt{y}H_1(iy)]_{y_1} & -\dfrac{\partial}{\partial z}[\sqrt{y}H_2(iy)]_{y_1} & 0 \\ 0 & H_1(iy_2) & H_2(iy_2) & -H_2(iy_2) \\ 0 & \dfrac{\partial}{\partial z}[\sqrt{y}H_1(iy)]_{y_2} & \dfrac{\partial}{\partial z}[\sqrt{y}H_2(iy)]_{y_2} & -\dfrac{\partial}{\partial z}[\sqrt{y}H_2(iy)]_{y_2}+\dfrac{\widehat{Ri}}{(1+c)^2}\sqrt{y_2}H_2(iy_2) \end{pmatrix}. \tag{C 13}$$

This yields the phase speed c. The coefficients A_1, A_2, B_2 and B_3 are then obtained when solving (C 10) and (C 11). After deriving the solution for ψ we easily obtain the vertical displacement $\zeta=\psi/(z-c)$ and the vorticity $q=-[Ri/(z-c)^2]\psi$.

Appendix D. Integrated kernel contribution to the momentum flux

We wish to express

$$\overline{uw}=\frac{1}{2\pi}\int_0^{2\pi}\mathrm{Re}(u)\mathrm{Re}(w)\mathrm{d}(kx) \tag{D 1}$$

in terms of the inversion of the vorticity profile $q=Q(z)\exp\{i[kx+\alpha(z)]\}$. For clarity, we redefine the Green function to be the real, positive-definite and non-dimensional evanescent function, $\tilde{G}(z,z')=iG(z,z')=(1/2)\exp(-k|z-z'|)$, and use (2.3) to write

$$\mathrm{Re}(w)=\int_{z'}Q(z')\sin[kx+\alpha(z')]\tilde{G}(z,z')\,\mathrm{d}z', \tag{D 2}$$

where the sine in the integrand simply indicates that the induced vertical velocity is located a quarter of wavelength to the east of the inducing vorticity anomaly (figure 11). Similarly we can write that

$$\mathrm{Re}(u)=\mathrm{Re}\left(\frac{i}{k}\frac{\partial w}{\partial z}\right)=\frac{1}{k}\int_{z''}Q(z'')\cos[kx+\alpha(z'')]\frac{\partial}{\partial z}\tilde{G}(z,z'')\,\mathrm{d}z''. \tag{D 3}$$

Since $(\partial/\partial z)\tilde{G}(z,z'')>0$ for $z<z''$ and $(\partial/\partial z)\tilde{G}(z,z'')<0$ for $z>z''$, the integrand indicates that the induced zonal velocity anomaly below (above) the inducing vorticity anomaly is in phase (anti-phase). Substituting (D 2) and (D 3) into (D 1) we obtain after zonal integration

$$\overline{uw}=\int_{z'}\int_{z''}\frac{1}{2k}Q(z')Q(z'')\sin[\alpha(z')-\alpha(z'')]\tilde{G}(z,z')\frac{\partial}{\partial z}\tilde{G}(z,z'')\,\mathrm{d}z'\mathrm{d}z''. \tag{D 4}$$

It is clear from the integrand that a single kernel (where $z'=z''$) does not contribute to the momentum flux. Writing explicitly the Green function and its

https://doi.org/10.1017/S002211201000529X Published online by Cambridge University Press

derivative,

$$\left.\begin{aligned}\tilde{G}(z,z') &= \frac{1}{2}\begin{cases}\exp[-k(z-z')] & \text{for } z>z',\\ \exp[k(z-z')] & \text{for } z<z'\ ,\end{cases}\\ \frac{\partial}{\partial z}\tilde{G}(z,z'') &= \frac{k}{2}\begin{cases}-\exp[-k(z-z'')] & \text{for } z>z'',\\ \exp[k(z-z'')] & \text{for } z<z''\ .\end{cases}\end{aligned}\right\} \tag{D 5}$$

Then if $z''>z>z'$, the integrand yields $-(1/8)Q(z')Q(z'')\sin[\alpha(z'')-\alpha(z')]\exp[-k(z''-z')]$, which is independent of z and positive if the vorticity is tilted westward with height. Flipping between the dummy variables z' and z'' yields the same contribution, indicating that indeed $\overline{[u(z')w(z'')]}_z=\overline{[u(z'')w(z')]}_z$. If, however, $z>z''>z'$ or $z<z'<z''$, then flipping between z' and z'' yields an exact cancellation and hence zero contribution. Taking these considerations into account we obtain (4.4) as the explicit form of (D 4).

REFERENCES

Baines, P. G. 1998 *Topographic Effects in Stratified Flows*. Cambridge University Press.

Baines, P. G. & Mitsudera, H. 1994 On the mechanism of shear flow instabilities. *J. Fluid Mech.* **276**, 327–342.

Booker, J. R. & Bretherton, F. P. 1967 The critical layer for internal gravity waves in a shear flow. *J. Fluid Mech.* **27**, 513–519.

Bretherton, F. P. 1966 Baroclinic instability, the short wave cutoff in terms of potential vorticity. *Q. J. R. Meteorol. Soc.* **92**, 335–345.

Charney, J. G & Stern, M. E. 1962 On the stability of internal baroclinic jets in a rotating atmosphere. *J. Atmos. Sci.* **19**, 159–172.

Davies, H. C. & Bishop, C. H. 1994 Eady edge waves and rapid development. *J. Atmos. Sci.* **51**, 1930–1946.

Eady, E. T. 1949 Long waves and cyclone waves. *Tellus* **1**, 33–52.

Eliassen, A. & Palm, E. 1960 On the transfer of energy in stationary mountain waves. *Geophys. Publ.* **22**, 1–23.

Fjørtoft, R. 1950 Application of integral theorems in deriving criteria of stability for laminar flows and for the baroclinic circular vortex. *Geofys. Publ.* **17**, 1–52.

Goldstein, S. 1931 On the stability of superposed streams of fluids of different densities. *Proc. R. Soc. Lond.* A **132**, 524–548.

Harnik, N. & Heifetz, E. 2007 Relating over-reflection and wave geometry to the counter propagating Rossby wave perspective: toward a deeper mechanistic understanding of shear instability. *J. Atmos. Sci.* **64**, 2238–2261.

Harnik, N., Heifetz, E., Umurhan, O. M. & Lott, F. 2008 A buoyancy–vorticity wave interaction approach to stratified shear flow. *J. Atmos. Sci.* **65**, 2615–2630.

Hayashi, Y. Y. & Young, W. R. 1986 Stable and unstable shear modes of rotating parallel flows in shallow water. *J. Fluid Mech.* **184**, 477–504.

Heifetz, E., Bishop, C. H., Hoskins, B. J. & Alpert, P. 1999 Counter-propagating Rossby waves in barotropic Rayleigh model of shear instability. *Q. J. R. Meteorol. Soc.* **125**, 2835–2853.

Heifetz, E., Bishop, C. H., Hoskins, B. J. & Methven, J. 2004 The counter-propagating Rossby-wave perspective on baroclinic instability. Part I. Mathematical basis. *Q. J. R. Meteorol. Soc.* **130**, 211–232.

Heifetz, E., Harnik, N. & Tamarin, T. 2009 A Hamiltonian counter-propagating Rossby wave perspective of pseudoenergy in the context of shear instability. *Q. J. R. Meteorol. Soc.* **135**, 2161–2167.

Heifetz, E. & Methven, J. 2005 Relating optimal growth to counterpropagating Rossby waves in shear instability. *Phys. Fluids* **17**, 064107.

Holmboe, J. 1962 On the behaviour of symmetric waves in stratified shear layers. *Geofys. Publ.* **24**, 67–113.

https://doi.org/10.1017/S002211201000529X Published online by Cambridge University Press

Hoskins, B. J., Mcintyre, M. E. & Robertson, A. W. 1985 On the use and significance of isentropic potential vorticity maps. *Q. J. R. Meteorol. Soc.* **111**, 877–946.

Howard, L. N. 1961 Note on paper of John W. Miles. *J. Fluid Mech.* **10**, 509–512.

Knessl, C. & Keller, J. B. 1992 Stability of rotating shear flows in shallow water. *J. Fluid Mech.* **244**, 605–614.

Lindzen, R. S. & Barker, J. W. 1985 Instability and wave over-reflection in stably stratified shear flow. *J. Fluid Mech.* **151**, 189–217.

Lindzen, R. S. & Rambaldi, S. 1986 A study of over-reflection in viscous poiseuille flow. *J. Fluid Mech.* **165**, 355–372.

Lindzen, R. S. & Rosenthal, A. J. 1981 A WKB asymptotic analysis of baroclinic instability. *J. Atmos. Sci.* **38**, 619–629.

Lindzen, R. S. & Tung, K. K 1978 Wave overreflection and shear instability. *J. Atmos. Sci.* **35**, 1626–1632.

Metheven, J., Hoskins, B. J., Heifetz, E. & Bishop, C. H. 2005 The counter-propagating Rossby-wave perspective on baroclinic instability. Part IV. Nonlinear life cycles. *Q. J. R. Meteorol. Soc.* **131**, 1425–1440.

Miles, J. W. 1961 On the stability of heterogeneous shear flows. *J. Fluid Mech.* **10**, 496–508.

Rayleigh, Lord 1880 On the stability, or instability, of certain fluid motions. *Proc. Lond. Math. Soc.* **9**, 57–70.

Sakai, S. 1989 Rossby–Kelvin instability: a new type of ageostrophic instability caused by a resonance between Rossby waves and gravity waves. *J. Fluid Mech.* **202**, 149–176.

Shepherd, T. G. 1990 Symmetries, conservation laws, and Hamiltonian structure in geophysical fluid dynamics. *Adv. Geophys.* **32**, 287–352.

Sneddon, I. N. 1956 *Special Functions of Mathematical Physics and Chemistry*. Oliver and Boyd.

Taylor, G. I. 1931 Effect of variation in density on the stability of superposed streams of fluid. *Proc. R. Soc. Lond.* A **132**, 499–523.

https://doi.org/10.1017/S002211201000529X Published online by Cambridge University Press